Electron-Phonon Coupling and Deep Conduction Band Resonance in Metal Halide Double Perovskites

Julian A. Steele,[1, a)] Pascal Puech,[2] Masoumeh Keshavarz,[3] Ruo Xi Yang,[4] Subhasree Banerjee,[3] Elke Debroye,[3] Cheol Woong Kim,[3] Haifeng Yuan,[3] Ho Heo,[5] Johan Vanacken,[6] Aron Walsh,[4, 7] Johan Hofkens,[3] and Maarten B. J. Roeffaers[1]

[1)] *Centre for Surface Chemistry and Catalysis, KU Leuven, Celestijnenlaan 200F, Leuven, 3001, Belgium*

[2)] *CEMES, Université de Toulouse, CNRS, 29, rue Jeanne Marvig, 31055 Toulouse, France*

[3)] *Department of Chemistry, KU Leuven, Celestijnenlaan 200F, Leuven, 3001, Belgium*

[4)] *Department of Materials, Imperial College London, Exhibition Road, London SW7 2AZ, United Kingdom*

[5)] *Department of Applied Chemistry, School of Applied Chemical Engineering, College of Engineering, Kyungpook National University, Daegu 41566, Korea*

[6)] *INPAC-Institute for Nanoscale Physics and Chemistry, KULeuven, Celestijnenlaan 200 D, B-3001 Leuven, Belgium*

[7)] *Global E3 Institute and Department of Materials Science and Engineering, Yonsei University, Seoul 120-749, Korea*

(Dated: 26 March 2018)

The properties of room-temperature conduction electrons in metal halide perovskites will be governed by intrinsic phonon scattering mechanisms and the electronic band-structure, and will define the carrier mobility and excitation/emission properties. Establishing how charge carriers interact within this scenario is fundamental for developing high-efficiency materials for opto-electronic applications. Herein we evaluate the electron scattering properties and conduction band environment in the lead-free double perovskite $Cs_2AgBiBr_6$ via a combinatorial approach; single crystal x-ray diffraction, temperature dependent emission spectroscopy, excitation and Raman scattering spectroscopy, with support from first principals calculations. We discover energy levels existing deep within the conduction band of $Cs_2AgBiBr_6$ and that scattering from longitudinal optical phonons – via the Fröhlich interaction – dominates electron scattering at room temperature, dwarfing the scatting from acoustic phonons, combining within the nominally non-resonant Raman scattering spectrum as mutliphonon processes up to the fourth order. A Fröhlich coupling constant of 82 meV is measured from a temperature dependent linewidth analysis of pure-phase $Cs_2AgBiBr_6$ double perovskite and is found to be relatively large when compared to common organolead perovskites (40 - 60 meV), or what we estimate from first principals. The origin of large Fröhlich interactions in $Cs_2AgBiBr_6$ is shown to be a consequence of phase impurity issues for which the solution processing of $Cs_2AgBiBr_6$ suffers, explains its poor carrier mobility, and we conclude that these findings are a general consequence of a disorder-prone metal halide double perovskite architecture.

Keywords: Double Perovskite, $Cs_2AgBiBr_6$, Fröhlich interactions, Raman scattering

Owed to their facile processing, low cost and appealing optical properties, the past decade has played witness to metal-halide perovskites (with general chemical formula ABX_3) encompassing one of the fastest growing materials ever seen within optoelectronics research[1]. In terms of their physical properties and optoelectronic performance, the organolead halide-based systems are championing this pursuit; as a vivid example, single-junction solar cells based on the $FAPbI_3$ perovskite (where FA is $HC(NH^2)^{2+}$) have achieved conversion efficiencies surpassing 22%[2] in just a few years, rivalling well-established Si-based technologies[3].

Initially motivated by a desire to move away from toxic Pb-based compounds, the perovskite catalogue was recently expanded to include lead-free, so-called, "double perovskite" systems, based on a $A^I_2B^IB^{III}X_6$ architecture[4]. This new branch is offering interesting and varied physical properties, differing substantially from their Pb-based counterparts. From its conception, the highly stable[5,6] all-inorganic $Cs_2AgBiBr_6$ system quickly became a popular material for researchers[7] [all refs]. With research interest for its application within multi-junction solar cells currently waning[8], its immediate promise seems reside in its strong potential for creating highly sensitive direct-conversion X-ray detectors[6].

$Cs_2AgBiBr_6$ is an indirect bandgap material, requiring phonon-assisted energy transitions between the valence band maximum (VBM) and conduction band minimum (CBM). Slavney *et al.*[9] recently reported on the indirect-direct gap of $Cs_2AgBiBr_6$, identifying phonons with an assisting energy of $\hbar\omega = 0.12$ eV are likely involved to bridge the momentum gap between the Γ and

[a)] Electronic mail: julian.steele@kuleuven.be

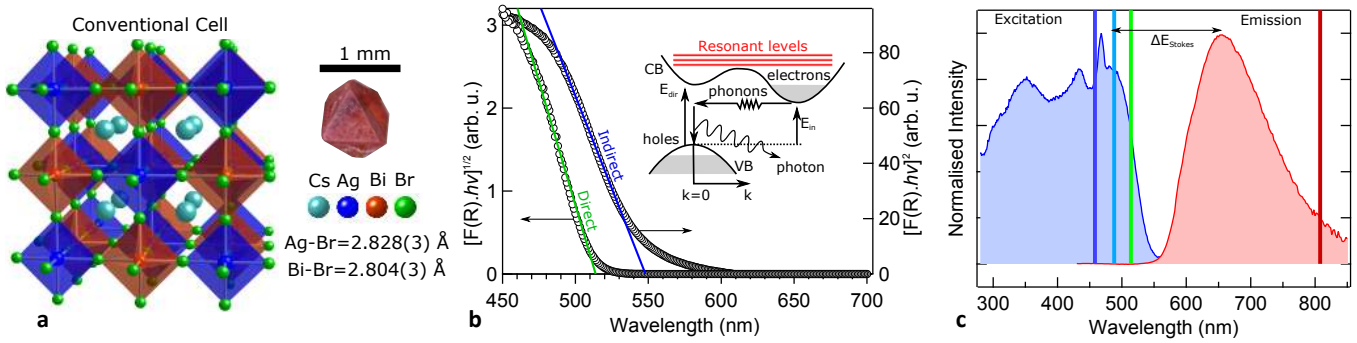

FIG. 1. **Structural and optical properties of phase-pure single crystal $Cs_2AgBiBr_6$.** (**a**) Optical image of a typical millimeter-sized single crystal (right) and the lattice structure of single crystal $Cs_2AgBiBr_6$ (left) derived from single crystal XRD analysis, along with the measured bond lengths for the Ag-Br and Bi-Br type bonds (numbers in parentheses here indicate the respective error values). (**b**) Tauc plot used to measure the indirect and direct bandgap via kubelkamunk functions. The inset shows the optical absorption process for an indirect bandstructure, complete with the CB resonant levels revealed through this work. (**c**) Normalized excitation spectra and emission spectra of both $Cs_2AgBiBr_6$ ($\lambda_{exc} = 400\,nm$ and $\lambda_{em} = 650\,nm$) and $CsPbBr_3$ ($\lambda_{exc} = 385\,nm$ and $\lambda_{em} = 450\,nm$) single crystals recorded at 300 K. For reference, the coloured vertical lines drawn through the spectra here indicate three excitation wavelengths used in (non-)resonant Raman scattering measurements shown in Figures 3 and 4.

L zone boundaries. Such a phonon band would possess a frequency nearing $1000\,cm^{-1}$, indicating that multi-phonon processes are at play here, defining its absorption edge[9]. Moreover, several recent theoretical studies of $Cs_2AgBiBr_6$[10,11] have suggested a complex conduction band (CB) energy landscape, where orbital-induced levels from both Bi and Ag atoms might disrupt the density of state (DOS) high into the CBM. How these orbitals might manifest through its opto-electronic properties is currently unknown.

The atoms of the room-temperature $Cs_2AgBiBr_6$ lattice are, however, not at rest and their relative displacements away from equilibrium positions perturbs the periodic potential acting on carriers, leading to carrier-lattice interactions. Conversely, a charge carrier together with its self-induced polarisation in the polar semiconductor forms a quasi-particle, which is called a polaron. The mechanisms of phonon scattering will underpin several important physical properties, like charge-carrier mobility, Stokes shift and emission linewidth, as well as limit thermal conductivity[12,13]. Beyond these better-known influences, it is further thought that the formation of large polarons in metal-halide perovskites[14–16] which are capably of internally screening each other might in fact slow down the carrier recombination process, helping to explain the relatively prolific reporting of long carrier lifetimes across many different systems [refs]. Note that for the pertinent case of room-temperature $Cs_2AgBiBr_6$, a relatively long radiative lifetime of roughly 660 ns was reported[9]. Needless to say, establishing how charge carriers interact with phonons is essential for the development of high-efficiency devices based on $Cs_2AgBiBr_6$. Thus far, intense efforts have been made for deciphering these interactions within popular lead-based perovskite systems[2,14,17–22] and despite the importance of carrier-phonon interactions to the optoelectronic properties, clear descriptions of what scattering mechanisms are active within lead-free double perovskites are yet to appear.

This we remedy in the following communication and shed light on the complex interconnectedness of the structural, vibrational and opto-electronic properties of high-quality single crystals of the double perovskite $Cs_2AgBiBr_6$. Using a combination of fine-structure x-ray diffraction (XRD) analysis, several optical spectroscopies and density functional theory (DFT) calculations, we outline a physical model which is characterised by giant electron-phonon coupling (so-called Fröhlich interactions) that arise via a highly harmonic and vibrationally dominate $(AgBr_6)^{5-}$ sublattice, as well as a collection of strongly resonant electronic states distributed above the CBM. In the appropriate places, we make direct comparison to the properties exhibited by popular Pb-based perovskites, highlighting the intrinsically novel nature of conduction electrons in double perovskite $Cs_2AgBiBr_6$.

RESULTS

We begin with an overview of the important characteristic properties of phase-pure[5] $Cs_2AgBiBr_6$. In the present work, we have chosen to study large mm-sized phase-pure single crystals of $Cs_2AgBiBr_6$ exhibiting model physical characteristics in the presence of no grain boundaries. It follows that, while $Cs_2AgBiBr_6$ appears to suffer from several growth generated defects, our pure-phase materials offer a preferable test bed for the evaluation of intrinsic properties.

Structural and optical characterisation $Cs_2AgBiBr_6$ single crystals (Figure 1a) were grown via the method reported previously[9]. Fine-structure single crystal XRD analysis was carried out using synchrotron X-radiation, with the structural analysis further

shown in Figure 1a, revealing a highly crystalline and phase-pure octahedral structure (space group $Fm\bar{3}m$), in sound agreement with the literature[9,23]. Note that the complete set of structural details (Table S1) and thermal and occupancy parameters (Table S2) derived can be found in the Supporting Information. The fundamental optical absorption edge was probed by UV-Vis diffuse reflectance spectroscopy, with the analysed spectra converted in Figure 2a via the Kubelka-Munk functions, F(R). Assessing the degree of linearity of our data scaled using both indirect-Tauc ($[F(R).h\nu]^{1/2}$ vs nm) and direct-Tauc ($[F(R).h\nu]^2$ vs nm) plots, we determine the respective bandgap transitions to be 550 nm (2.25 eV) and 514 nm (2.41 eV). The value of the indirect bandgap is comparable to other reports which range from 677 nm (1.83 eV) to 566 nm (2.19 eV)[5,8,23–25]. Isolating the origin(s) of the relatively large spread in E_g values observed here is difficult, although the answer likely resides in the different methods employed to probe the materials band structure which exhibits an extremely large Stokes shift (see Figure 2b) and the variances in synthesis conditions. Recent work by Yang *et al.*[26] has suggested that the ordering parameter in the double perovskite can lead from a larger indirect bandgap (fully ordered) to a smaller pseudo-direct one (fully random ordering). Thus, combined with the narrow growth window of $Cs_2AgBiBr_6$[27], a wider bandgap is concomitant with a more ordered system with less Ag-on-Bi (Ag_{Bi}) or Bi-on-Ag (Bi_{Ag}) antisites[6].

Next we study the properties of photo-generated states in $Cs_2AgBiBr_6$ by assessing its excitation and steady-state photoluminescence (PL) spectra, which is shown in Figure 2b. The PL spectrum of $Cs_2AgBiBr_6$ here exhibits a wide and smooth emission centred near 650 nm, while the excitation spectrum is characterised by a very broad response, suggesting multiple photo-excited states that are widely distributed in energy. Moreover, the excitation lineshape – with the inclusion of sharp peak-like features – further suggests some of these states to be discrete-like, existing above the absorption edge and well into the CB. This is in direct contrast to typical excitation spectra, being relatively smooth, containing only a singular excitation peak and exhibiting a smaller Stokes shift energy (ΔE_{Stokes}). On the origin of the above bandgap energy levels in $Cs_2AgBiBr_6$, several recent reports[10,11] provide sound theoretical support for their discussion. In short, density functional theory (DFT) calculations accounting for the influence of spin-orbit coupling have indicated that the CBM of ordered[26] $Cs_2AgBiBr_6$ is composed mainly of 6p orbitals, with some additional contributions from the Ag 5s and Br 4p orbitals[10]. This electronic structure governs the energy landscape for which photo-generated electrons can be excited from the ground state into the CB, where these orbitals are further split due to spin-orbit coupling[10]. Electronic transitions in the $Cs_2AgBiBr_6$ will couple to lattice vibrations, acting to broaden the emission band and enlarge the Stokes shift energy, E_{Stokes}. Together, the relatively large Stokes shift and large emission linewidth seen in $Cs_2AgBiBr_6$ is a strong indicator of significant Fröhlich coupling strength within this material.

Vibrational Properties. To evaluate the nature of phonon vibrations in $Cs_2AgBiBr_6$, its lattice dynamics were calculated using density functional theory (DFT) via the PBEsol exchange-correlation functional and a hamornic approximation (anharmonicity not considered), with the determined zone centre phonon DOS for $Cs_2AgBiBr_6$ presented in Figure 3a. Jahn-Teller distortions constitute a good portion of the vibrational states seen here, which is common for a highly-mobile perovskite structure. Unsurprisingly, given the relatively heavy elements involved here, the first-order phonons contain only relatively low-energy vibrations, all residing far bellow 200 cm^{-1} (note that the DFT calculation determined properties at 0 K, so frequencies measured at room temperature will be inherently larger).

For the vibrational analysis of the $Cs_2AgBiBr_6$ crystal structure (O_h symmetry), parallels can be drawn to other analogous elpasolite perovskites; see inset of Figure 3b. A complete factor group analysis is developed on the basis of the Bravais cell, which is used to predict the vibrational symmetries of $Cs_2AgBiBr_6$ (see Table S3 of Supporting Information). Analysing the XRD data in Figure 1b to assess the relative internal forces of the two competing $(AgBr_6)^{5-}$ and $(BiBr_6)^{3-}$ octahedral bonds, we find that the relative strength of the Ag-Br and Bi-

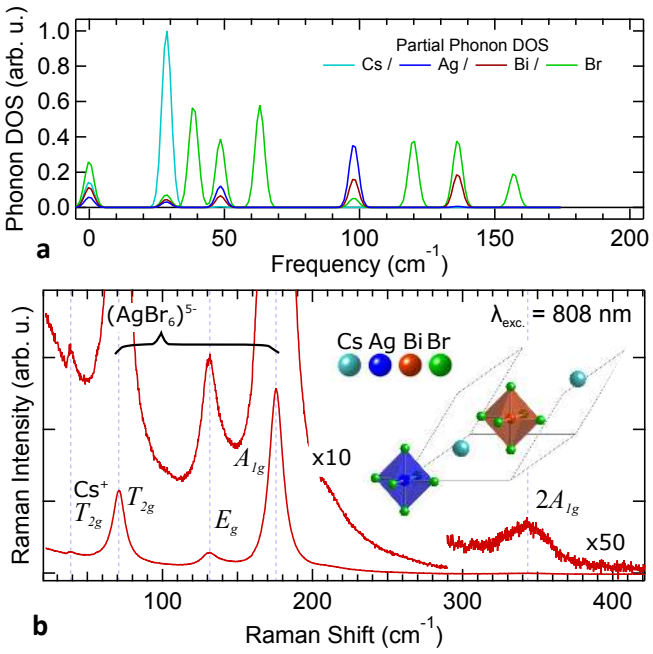

FIG. 2. **Lattice dynamics of $Cs_2AgBiBr_6$.** (**a**) DFT calculation of the partial phonon DOS at the zone center (Γ) for $Cs_2AgBiBr_6$ at 0 K, using a smearing factor of 2 cm^{-1}. (**b**) Non-resonant Raman spectrum recorded using 808 nm excitation, with the inset showing a representation of the primative cell, whereby the two octahedral sublattices are separated.

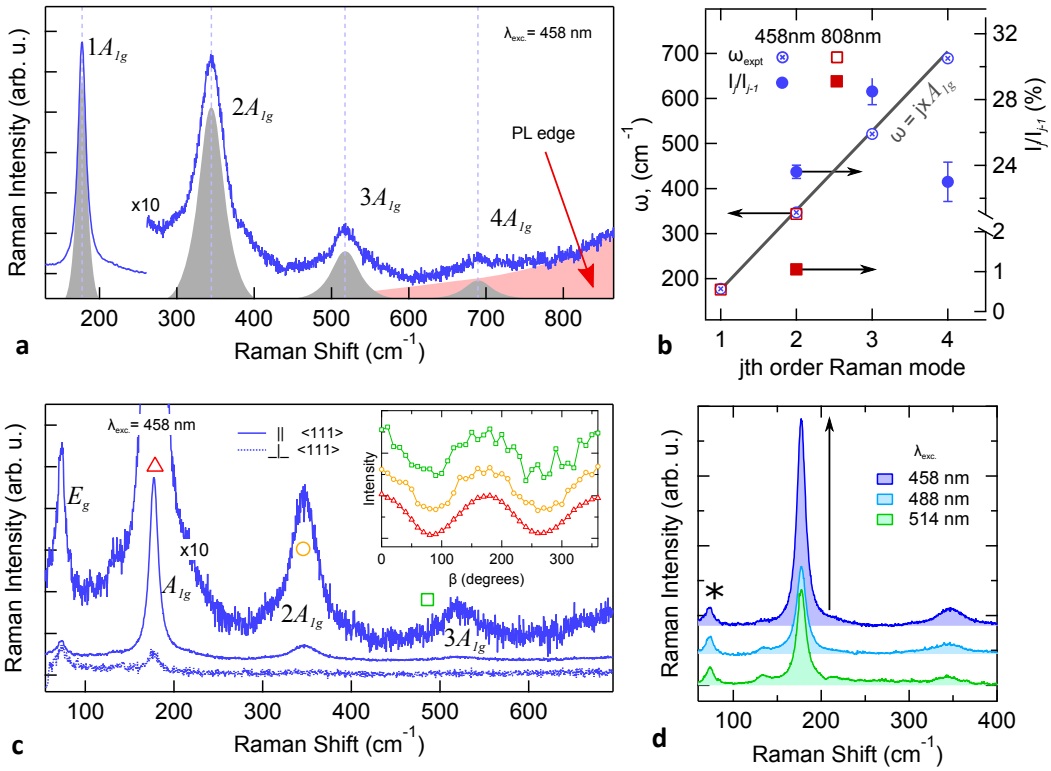

FIG. 3. **Quasi-Resonant and polarised Raman scattering studies of $Cs_2AgBiBr_6$.** (**a**) Unpolarised Raman spectrum recorded using 458 nm excitation, highlighting observations of up to the fourth A_{1g} harmonic, before Raman signals are lost the the high-energy shoulder of the PL emission. (**b**) Frequency and relative intensity harmonic Raman modes. (**c**) Comparison of polarised Raman back-scattering spectra recorded using 458 nm excitation and polarising optics parallel and perpendicular to the <111> crystal direction, with the full analysing rotation data made with a the polarisation of the incident light fixed along <111>. The traces in the inset have been offset and normalised for clarity. (**d**) Comparison of pseudo-resonant Raman scattering effect (normalised to mode at 75 cm^{-1}, indicted by "*") made with three different excitation energies across the absorption edge (see positions of excitation relative to excitation spectrum in Figure 2b).

Br bond types strongly differ. This is concluded from a comparison to the measured bond lengths (see Figure 1c) and their calculated ionic radii: for the 6-coordinated B-Br types (B= Bi or Ag), we have Bi-Br= 2.99$\mathring{A}$ and Ag-Br= 2.99$\mathring{A}$. In this way, the bonding strength of the Ag-Br type bonds are found to be much stronger than the Bi-Br ones, permitting it to be considered a discrete-like entity. In such a scenario the $(AgBr_6)^{5-}$ lattice vibrations dominate and $(BiBr_6)^{3-}$ Raman modes turn silent. It follows that 4 active first-order modes are anticipated in the non-resonant Raman scattering spectrum. These vibrational modes consist of a single low-energy vibration which is a translational mode due to the "caged" Cs^+ ions, and 3 higher energy modes corresponding to a single breathing and two stretching vibrations arising from the $(AgBr_6)^{5-}$ sublatttice.

The room-temperature non-resonant Raman spectrum measured using 808 nm laser light is presented Figure 3b, with the relative wavelengths used for Raman excitations within this paper indicated in Figure 2b via the red vertical line. Here we see a total of 4 bands below 200 cm^{-1}, as expected from our group factor and fine-structure analysis, with their intensity and frequency in complete agreement with that measured from analogous elpasolite systems[28–30]. According to our assignment, the narrow low frequency band at 40 cm^{-1} is ascribed to the T_{2g} mode of the Cs^+ ions, while the 3 other more intense bands at 75, 135 and 175 cm^{-1} belong respectively to the T_{2g} (breathing), E_g and A_{1g} (both stretching) modes of the $(AgBr_6)^{5-}$ octahedron, given that the following general relation[30] is satisfied: $v^2_{A_{1g}} \approx v^2_{E_g} + \frac{3}{2}v^2_{T_{2g}}$.

The $Cs_2AgBiBr_6$ double perovskite system remains to exhibit phase purity issues, mainly due to its narrow growth window and a tendency to form a Bi-rich yellow-coloured material[7]. During the optimisation stage of producing our pure-phase $Cs_2AgBiBr_6$ materials, the yellow phase was on occasion inadvertently synthesised, and we provide its characterisation using energy-dispersive X-ray spectroscopy (Figure S2; showing the material to be Bi-rich) and Raman spectroscopy (Figure S3; identifying its unique Raman modes) in the Supporting Information. Where XRD unavoidably requires bulk characterisation and might potentially miss the presence of small trace amounts of the second yellow phase, we emphasise that the vibrational signatures of the yellow phase will provide a relatively straight forward and reliable probe for eval-

uating localised deviations in phase purity within single crystals. Note we offer a powerful demonstration of this approach later on.

Phonon Coupling and the Stokes Shift In polar semiconductors, an important scattering mechanism is the Fröhlich interaction, which represents the coupling of longitudinal optical (LO) phonons to lattice vibrations via Coulomb interactions. Here we identify the LO phonon to have A_{1g} symmetry and an energy of $\hbar\omega_{LO} = 175\,cm^{-1}$, whereby the Fröhlich interaction should dominate at room temperature[19] given the LO phonon occupation number is high; $k_B \gg \hbar\omega_{LO}$. The interactions between optical centers and LO modes may be characterised by the Huang-Rhys factor, S, which represents (i) the average number of vibrations emitted after optical transition between excited and ground states, and (ii) an indicator of the coupling strength. The Hung-Rhys parameter follows the standard form of a configuration coordinate diagram and is approximately[31] related to the Stokes shift energy via $\Delta E_{Stokes} = 2S\hbar\omega_{LO}$ Using the measured energy shift seen between the emission and excitation bands of $Cs_2AgBiBr_6$ in Figure 2a (i.e., $\Delta E_{Stokes} \sim 0.7\,eV$), we arrive at the relatively large Huang-Rhys value of S = 15.4.

Higher order Raman active harmonics. Interestingly, in the non-resonant 808 nm excited Raman spectrum shown in Figure 3b, an additional weak band is clearly resolved at higher energies on the ×50 re-scaled portion of the trace. With no high-energy modes expected from the first-order phonon density of states calculated in Figure 3a, such a band likely arises from higher order combinations of LO phonons (A_{1g}-type). Assessing its observed vibrational energy to be $346\,cm^{-1}$, we find it to reside just short of double the A_{1g} mode at $175\,cm^{-1}$, indicating it indeed has a strong $2A_{1g}$ component. We note that non-resonant overtones is not unexpected in polar crystals which exhibit relatively large carrier-phonon coupling, but is actually unusual within the more modern non-oxide perovskites.

To examine if the $346\,cm^{-1}$ mode comes from second-order scattering of A_{1g} phonons, we evaluate its Raman response using highly absorbing above-bangap 458 nm excitation (see Figure 2b) and search for the possible addition of higher order bands. In Figure 4a we present the higher energy portion of the Raman spectrum recorded using a relatively low laser power density to avoid laser damage (Figure RRS) and highlight observations of high-energy modes nearing toward $700\,cm^{-1}$. In the inset, the recorded frequencies of the j-th order modes are compared to that expected from their respective harmonic A_{1g} combinations. The position of these bands are in good agreement with the predicted overtones, all the way up to a stunning *fourth order* observation. The recorded values here do deviate slightly, being in the vicinity of 2 to 3% less than their respective first-order A_{1g} multiples, suggesting vibrational contributions to centrally come from the Γ point[32]. As well, the relatively large broadening of the higher order peaks (a full width half maximum of roughly $10\,cm^{-1}$ at $j = 1$, to roughly $40\,cm^{-1}$ at $j = 2, 3$ and 4) and its relative deviation towards lower frequencies both suggest additional contributions of A_{1g} phonons from other points of the Brillouin zone[13]; the participation of ordinarily forbidden $k \neq 0$ phonons in these multiphonon processes might explain their relatively large widths.

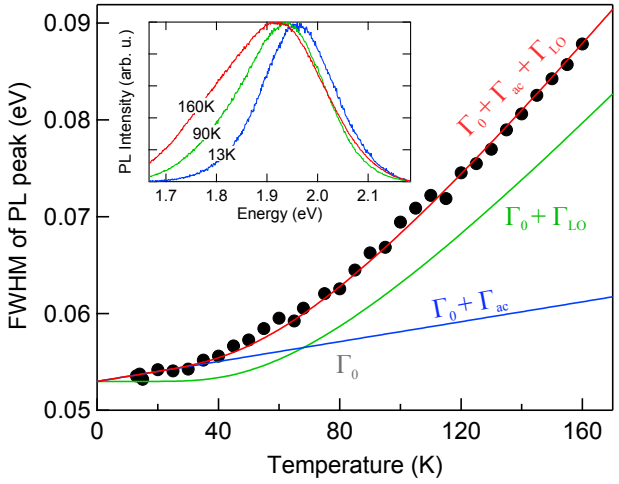

FIG. 4. **Temperature dependence of $Cs_2AgBiBr_6$ emission linewidth.** FWHM of single crystal $Cs_2AgBiBr_6$ steady-state PL spectra as a function of temperature, with an example of measured raw data spectra provided in the inset for several different temperatures. The red line is a fit made with Eq. 1 using the parameters $\Gamma_0 = 183\,meV$ and $\hbar\omega_0 = 22\,meV$, while the measured contributions to the linewidth broadening induced by acoustic and LO phonon (Fröhlich interactions) coupling are parsed via the blue and green traces, respectively.

Next we unambiguously confirm the common vibrational symmetry of these modes via the Raman back-selection rules and through implementing polarised Raman measurements. Polarising the incident light along the <111> direction of a $Cs_2AgBiBr_6$ single crystal, and analysing polarised scattered light rotated around the (111) plane (forming the relative polarisation angle β), constitutes the data shown in Figure 4a. First, at polarisation geometries both parallel ($\beta = 0$) and perpendicular ($\beta = 90°C$) to the <111> crystallographic direction, oscillators identified by combinations of A_{1g} are all active and non-active, respectively, confirming their shared symmetry. The full rotation analysis of this measurement is also contained in the inset of Figure 4a, where the normalised and offset intensity of the three modes are shown to coincide throughout the full rotation, confirming this.

On the scaling used to present the Raman data in Figure 4a and b, it is clear that the relative oscillator strength of the consecutive overtones are large, and substantially larger than that measured using 808 nm excitation (see Figure 2b). The selective nominally non-resonant enhancement of optical overtones indicates the presence of relatively strong electron-phonon Fröhlich

interactions[33] within $Cs_2AgBiBr_6$. This is qualified in the inset of Figure 4a, where the intensity of the jth mode (I_j) is compared relative to $j-1$ (I_{j-1}), and is roughly 1% when using 808 nm light and jumps closer to 30% when using above bangap 458 nm excitation, up to the recorded fourth order mode. We point out this trend explicitly overshoots theoretical considerations for such Raman multiphonon behaviour[34] and is in fact a central parameter leading to the spectroscopic quantification of an extremely large carrier-phonon coupling strength[17,33]; the intensity if the second order mode relative to the first will be directly proportional to the Haung-Rhys parameter, S. Note that the semiconductor response to the excitation laser energy used significantly complicates an analysis of the carrier-phonon coupling strength here and a more detailed examination in still to come later. As such, a spectral analysis breaks down due to the strong emergence of third-order and fourth-order A_{1g} bands, suggesting the occurrence of resonance effects, while its excitation energy relative to the CBM in Figure 2b – being well above it – does not. Presumably the higher order overtones arise here from resonant conditions being somewhat satisfied, in the presence of deep conduction band energy levels.

In Figure 4c the influence of varying the Raman excitation energy is examined. While typical resonant Raman scattering experiments aim to match the excitation energy with a fundamental interband transitions of the semiconductor, here we aim to probe resonant levels deep within the CB of $Cs_2AgBiBr_6$. For the change in excitation conditions, we point out that negligible spectral changes are seen for different populations of photo-injected charge carriers and all measurements were performed using a low laser power density. Compared to the excitation spectrum recorded in Figure 1b, the relative position of the exciting 458 nm, 488 nm and 514 nm photons are indicated by the vertical lines. Unpolarised Raman data are recorded at these wavelengths and are compared in Figure 4b via a normalisation to their respective E_g symmetry vibrations near 75 cm^{-1}. For these data, a correction has been applied to the spectral background for those recorded using 488 nm and 514 nm light, given their relative proximity to the high-energy shoulder of the PL emission which defines the background (Figure S4 in the Supporting Information). In doing so, we see a substantial rise in the relative scattering cross-section of the A_{1g} and $2A_{1g}$ modes of the $(AgBr_6)^{5-}$ octahedra, relative to the E_g band, when employing different photon energies traversing the absorption edge (see Figure 2b). The relative weightings of both the A_{1g} and $2A_{1g}$ roughly triple here when moving from 488 nm to 458nm. In fact, from the charge density isosurface calculations reported by Savory et al.[8], the electron density in the CB is mainly localized near the metal atoms of the crystal lattice, providing efficient electron-phonon coupling to orbit-induced levels. Further, through an analysis of the relative weights of the second and first order bands we find there is also a sharp spike in the relative overtone intensity when moving from 514 nm (0.11) to 488 nm or 458 nm (both being ~ 0.25). Being directly proportional to the Huang-Rhys coupling strength, S, this variation in the relative weight of the second order band reflects a large change in the coupling strength and signifies an energetically local shift in the resonance conductions. Together, this verifies the notion of photo-generated electrons being promoted directly into discrete-like states well above the CBM.

Temperature dependence of PL emission linewidth. To quantify the relative activity of different charge-carrier scattering mechanisms in $Cs_2AgBiBr_6$, we investigate the temperature dependence of the emission linewidth, which constitutes the data presented in Figure 4. To provide details useful for its analysis, a comparison of the Raman spectrum of $Cs_2AgBiBr_6$ recorded at 80 and 300 K (808 nm excitation) is presented presented in Figure S5 of Supporting Information. Via this comparison, very little spectral differences are seen, indicating the elpasolite structure is persevered at lower temperatures, extending a practical application of our analysis up to room temperature. Further, we exact the energy of the low-temperature optical phonon involved, i.e., $\hbar\omega_{LO}$ is measured to be 22 meV (177 cm^{-1}).

Heading to lower temperatures in Figure 4, the PL emission narrows significantly from FWHM = 88 meV at 150 K down to 53 meV at 13 K, as highlighted by the PL spectra contained in its inset. Such a monotonic dependence on temperature is relatively well understood for semiconducting materials[19,35] and is compactly described by the Eq. 1 below, where we have chosen to adopt the nomenclature used by Wright *et al.*[19]. Within the broadening model implemented in our work – where we ignore the negligible trend of scattering from ionised impurities[19,36], which is not expressed in our data – two central temperature-dependent parameters act functionally different to widen the emission linewidth above absolute zero, being described by

$$\begin{aligned}\Gamma(T) &= \Gamma_0 + \Gamma_{ac} + \Gamma_{LO} \\ &= \Gamma_0 + \gamma_{ac}T + \gamma_{LO}N(T).\end{aligned} \quad (1)$$

Here Γ_0 is a constant and represents the temperature-independent inhomogenous broadening parameter originating due to scattering from disorder and/or crystallographic imperfections. The next two terms provide the important temperature dependence: Γ_{ac} and Γ_{LO} are the acoustic and optical phonon (Fröhlich) interactions with carrier-phonon coupling constants γ_{ac} and γ_{LO}, respectively. Given the LO phonon energy in $Cs_2AgBiBr_6$ is over 20 meV, its population below 100 K will be small, being governed by the Bose-Einstein distribution $N(T) = 1/\exp(\hbar\omega_0/k_BT-1)$. Thus, one can expect that the emission broadening in this temperature regime will contain significant contributions from the scattering of acoustic phonons[37]. In parsing the two contributions to broadening, we find the best fits to our data are made accounting for the γ_{ac} at the low temperature regime. Extrapolating the data in Figure 4c to 0 K we estimate a relatively

large[19] natural linewidth of $\Gamma_0 = 52.8 \pm 0.5\,\text{meV}$, suggesting a substantial intrinsic defect population.

Inputting these parameters into Eq. 1 one arrives at the following electron coupling constants: $\gamma_{\text{ac}} = 55 \pm 6\,\mu\text{eV}$ and $\gamma_{\text{LO}} = 82 \pm 8\,\text{meV}$. Note that relatively large error margins manifest here due to both a strong dependence on our extrapolation of Γ_0 to 0 K and the fact that only the temperature range is limited to values only as low as down to 13 K; we provide a clear representation of this variance in Figure S6 of the Supporting Information. Nonetheless, the data are sufficiently clear in revealing that a relatively large electron-phonon Fröhlich interaction within $Cs_2AgBiBr_6$, being 1.5 to 2 times larger than that reported by Wright[19] for several popular organic Pb-based systems; namely, the four variants of (FA,MA)Pb(I,Br)$_3$, having γ_{LO} values in the order of 40 to 60 meV.

From our data, it can be concluded that Fröhlich coupling to LO phonons is the major cause of linewidth broadening in $Cs_2AgBiBr_6$ at room temperature, with scattering from acoustic phonons and impurities being far less important. This result is in complete agreement with a classic band-structure picture for a polar inorganic semiconductor, as well aligning well with hybrid Pb-based perovskites[19].

Fröhlich Interaction From First-Principals: For comparison, we assess the carrier-LO-phonon coupling strength from first-principals; in polar semiconductors the full electron-phonon coupling problem can be approximated by interaction of carriers with a long-wavelength longitudinal optical phonon as described by the unitless Fröhlich parameter, α. This parameter is one component of the coupling strength and has been used as a comparative indicator for the Fröhlich interaction strength[22,38]. Here we adopt the approach detailed by Frost[22] for calculating the Fröhlich coupling strength of both electrons and holes in $Cs_2AgBiBr_6$:

$$\alpha = \frac{1}{4\pi\epsilon_0}\frac{1}{2}\left(\frac{1}{\epsilon_\infty} - \frac{1}{\epsilon_{\text{S}}}\right)\frac{e^2}{\hbar\Omega}\left(\frac{2m_{\text{b}}\Omega}{\hbar}\right)^{1/2}. \qquad (2)$$

Here ϵ_∞ is the optical dielectric constant, ϵ_{S} is the static dielectric constant, m_{b} is the carrier effective mass and respectively is taken[39] for electrons and holes as 0.29 and 0.47, and Ω is the characteristic phonon angular frequency. Parameters ϵ_∞ and ϵ_{S} have been calculated using density functional perturbation theory ($10 \times 10 \times 10$ k-point and 800 eV plane-wave cut-off) and determined to be 5.42 and 16.73, respectively. For the effective phonon frequency, we have the Hellwarth scheme to sum over the infrared activity of all phonon branches[22,40] and use the value 3.703 THz. Note that the phonon frequencies are calculated in harmonic approximation and exclude finite-temperature effects. At elevated temperatures, the effective phonon frequency can shift due to thermal expansion and anharmonicity due to population of higher energy modes. Through Eq. 2 we estimate the Fröhlich parameters for electrons and holes in $Cs_2AgBiBr_6$ to be 2.54 and 2.00, respectively. Relative to many other perovskite semiconductors, this calculation places the carrier-phonon coupling strength of $Cs_2AgBiBr_6$ well within the "intermediate" range[22] (see Frost[38] for a useufl comparison of this parameter across many different materials), and certainly not into a regime which can be identified as "large" or "strong".

The first-principals calculation of the carrier-phonon coupling strength is of course in direct conflict to the collective evidence outlined above, where a notably strong Fröhlich coupling strength in $Cs_2AgBiBr_6$ is revealed experimentally. In reconciling this difference, we find precedence for similar disagreements between experiments and theoretical calculations within the literature: the relative magnitudes of α values calculated by Frost[22] for perovskites $MAPbI_3$ (2.39) and $MAPbBr_3$ (1.69) are in reversed order when compared to the γ_{LO} coefficients experimentally measured by Wright[19] for the same material systems, being in this case $\gamma_{LO} = 40\,\text{meV}$ and 58 meV, respectively. This highlights the delicate nature by which first-principle calculations and experimental measurements may be compared for this problem.

The origin of the mismatch between theory and experiment likely resides in the fact that the crystal structure simulated in the calculations assumes the perfect ordering of Ag- and Bi-type sublattices (i.e. perfect chequerboard-like structure), where in reality there will be disorder and localised fluctuations in the electrostatic potential (i.e. via charged antisites or Bi-rich yellow areas), which can act to further enhance carrier-lattice coupling. Note that, with regards to the emission linewidth shown in Figure 4, large lattice disorder is strongly indicated by our determination of a relatively large[19,36] natural width of $\Gamma_0 \sim 53\,\text{meV}$.

Experimental Evaluation of Disorder-Based Model: To test the notion that lattice disorder – in the form of localised compositional deviations – influences Fröhlich interactions within this double perovskite, we apply a similar evaluation to that seen so far to a $Cs_2AgBiBr_6$ single crystal suffering from yellow Bi-rich (nano-)regions. In this way, the level of disorder will be relatively high compared to the quality materials studied until now, and should exhibit enhanced Fröhlich coupling. The characterisation took a dual approach; first, micro-Raman surface mapping confirmed the presence of localised areas of the yellow phase (Figure S7 of the Supporting Information) peppered throughout the $Cs_2AgBiBr_6$ single crystal, and second, the temperature dependence of the emission linewidth is evaluated (see Figure S8 of Supporting Information). In short, Γ_0 is measured to be substantially larger at $59 \pm 4\,\text{meV}$ (verifying the presence of enhanced disorder), little change is seen in γ_{ac} at 49 ± 4 ueV and a large shift is measured for the Fröhlich coupling strength, at $\gamma_{\text{LO}} = 89 \pm 6\,\text{meV}$. These finding provide support for the model described above, where the electron-phonon coupling strength within $Cs_2AgBiBr_6$ is strongly influenced by the degree of lattice ordering. Given the high purity of

the single crystal materials evaluated in Figure 4, we are confident that the coupling constant derived therefrom are close to nearing the $Cs_2AgBiBr_6$ intrinsic lower limits, using the synthesis protocol outlined in the Methods section.

In terms of crystal quality, the materials studied herein are solution processed, inheriting a collection of intrinsic limitations with respect to crystal quality, purity and something which plagues the perovksite family more generally; reproducibility. Needless to say, the latter point has been vividly revealed here in this paper. As such, we suggest that solid-state synthesis – through chemical vapour deposition[41], melt processing[42,43], or otherwise – should help mitigate these effects, which, as outlined in this paper, have far reaching consequences on double perovskite physical properties at the macro-scale.

Within the more general landscape of double perovskite materials, we expect this to be a fundamental and important structural difference between the single and double perovskites, and suggest similar phenomena might manifest elsewhere in perovskites possessing a dual metallic architecture, i.e. in which two sublattices thermodynamically compete during crystal growth. Further, it should be stressed that the occurrence of phonon coupling described here for $Cs_2AgBiBr_6$ has implications for inorganic as well as hybrid silver / bismuth halide perovskites, due to the participation of low-energy, octahedral phonon modes, which should not depend on the nature of the cation.

DISCUSSION

Within a technological context, the implications of this work are substantial. For the specific applications of $Cs_2AgBiBr_6$ for solar cells or light-emitting devices (LEDs), strong carrierphonon coupling typically leads to increased carrier scattering during transport and limits mobility at room temperature. Additionally, experimental and theoretical reports have recently proposed different mechanisms for charge carrier binding in lead halide perovskite materials, involving the self-trapping of electrons[44] or holes[45] through the formation of small polarons. Considering the implications of our model based on a disorderly double perovskite crystal lattice, this cannot be overlooked in accurately describing the transport properties of carriers in $Cs_2AgBiBr_6$ and may help explain its intrinsic p-type behaviour at room temperature[6]. As such, the measured carrier mobilities within $Cs_2AgBiBr_6$ are relatively low[6], likely leading to increased loss of carriers through non-radiative recombination and lowering overall device performance, as a result of reducing both the carrier injection and transport efficiencies. Moreover, the strong broadening of mission linewidths due to phonon coupling will have consequences for the colour purity of light emitters.

On the other hand, for applications such as x-ray detection[6], heavy-Z semiconductors with long carrier lifetimes and relatively high resistivities are in fact extremely desirable, for suppressing the dark current under exposure to extremely high external fields (100s of volts). Further, strong electron-phonon coupling was recently found to be fundamental in the production of THz radiation from perovskites following photoexcitation[46], offering new prospects for cheap and easy to make solid-state THz sources.

The implications of the deep conduction band resonance exhibited in $Cs_2AgBiBr_6$ single crystals is yet to be addressed. The nature of the energy levels is to locally modify the DOS for conduction electrons, moving toward a more discrete-like system. A likely consequence for electrons existing at resonance is to have their effective mass increased. Parallels can be drawn here to the ternary III-V semiconductor $GaAs_{1-x}N_x$ which also experiences resonance above the CBM, introduced via N-derived energy levels. In this case, an increase in the effective mass of conduction electrons is observed[47]. In $Cs_2AgBiBr_6$, an increase in the effective mass could help explain the relatively high order of Raman overtones seen in Figure 4a, in that the coupling strength will scale with the effective mass, through Eq. 2. Additionally, this will also impede the mobility of electrons residing at the orbital levels, however, their energies are – from a theoretical point of view[10] – relatively far from typical transport states existing at the CBM. Ultimately, the orbital-induced levels manifests as the anomalous energy-dependent spectroscopic features observed here and are typically not seen in other Pb-based perovskite semiconductors, which possess a "smoother" CB.

In summary, we have presented a detailed study on the excited states and phonon dynamics of phase pure $Cs_2AgBiBr_6$ single crystals.

Using DFT the first-order phonon density of states was calculated, revealing the full oscillator portfolio to fall well short of $200\,cm^{-1}$, suggesting mutliphonon combinations of a relatively high order are required for phonon-assisted optical absorption. A comparison of the non-resonant Raman spectrum measured at 808 nm with both the phonon density of states and a full group analysis of the $Cs_2AgBiBr_6$ structure allows for unambiguous spectral assignment of an non-typical spectra, defined by internal forces acting to silent $(BiBr_6)^{3-}$ contributions. Unusual multiphonon processes up the fourth order are observed in the nominally non-resonant Raman spectrum measured at 458 nm, with their common vibrational symmetry confirmed via polarisation measurements. Together, with excitation spectroscopy, such behaviour is assigned to resonance with orbital levels within the CB and strong carrier-phonon Fröhlich interactions. We speculate that an extremely flat optical branch of the A_{1g} phonon dispersion at the high-symmetry Γ point is required to give rise to its large phonon density of states, constituting another key factor to their vivid appearance. We conclude that the unusual physical properties exhibited herein should not be overlooked when fabricating photo-active devices from $Cs_2AgBiBr_6$.

Altogether, the results presented in this work provide a fundamental understanding of the properties of CsPbBr3 as a material with potential commercial applications.

METHODS

Synthesis of single crystal $Cs_2AgBiBr_6$. Materials were grown according to procedure reported by Slavney *et al.*[9]. A mixture of 1.0 mmol of BiBr3 (≥98%, Sigma-Aldrich) and 2.0 mmol of CsBr (99.9%, Sigma-Aldrich) in 10 mL of HBr (≥99.99%, 48 w%, Honeywell Fluka) in a 40 mL vial was sonicated for 5 minutes. After adding 1.0 mmol AgBr (≥ 99%, Chem-Lab), the suspension was sonicated a further 5 minutes and then heated to 120°C to dissolve the salts to a level of supersaturation. The mixture was kept at 120°C for 3 hours, then cooled by 2°C/h to 100°C, followed by slower cooling at a rate of 1C/h to 50°C. At that time, mm-sized single crystals could be observed and collected from the mixture by filtration. The crystals were washed with isopropanol and then dried in a vacuum oven at 50°C. Concentrated 2-propanol (HPLC, Sigma-Aldrich), dimethylsulfoxide (DMSO) (anhydrous, ≥99.9%, Sigma-Aldrich) and methanol (MeOH) (anhydrous, 99.8%, Sigma-Aldrich) were used without any dilution. The solvents were either of technical grade or higher quality. Synthesis was performed under normal atmospheric condition.

Single crystal x-ray diffraction. Diffraction intensities for the single crystal were measured with synchrotron X-radiation via a silicon (111) double crystal monochromator with 0.6300 Åwavelength. The BL2D-SMDC program was used for data collection by the omega scan method.1 Highly redundant data sets were harvested by collecting 72 sets of frames with a 5° scan and an exposure time of 1 s per frame. The HKL3000 program, including the automated indexing program DENZO, was used to prepare the basic data files. These were corrected for Lorentz and polarization effects; negligible corrections for crystal decay were also applied. For structure determination, full-matrix least-squares refinements (SHELXL2016) using the space group $Fm\bar{3}m$ were done using all unique reflections measured. Atomic scattering factors for neutral atoms and the atomic parameters of the previous literature were used initially[9]. Anisotropic thermal parameters for all atoms and fixed weights were applied.

UV-Vis diffuse reflectance spectroscopy. Diffuse reflectance spectra (DRS) were recorded in the wavelength range between 200 nm to 800 nm with a Perkin Elmer Lambda 950 UV-Vis spectrophotometer. As reference, $BaSO_4$ powder was used. Crystals were crushed to a very fine powder and placed in a quartz cuvette with 1 mm path length, sealed with a Teflon stopper. Cuvettes were mounted in an integrating sphere equipped with a spectrophotometer to align the incidental light beam perpendicular to the sample. The diffused reflectance (R) was converted to F(R) using the Kubelka-Munk function: $F(R) = (1-R)^2/2R$.

Emission and Excitation Spectroscopy. Emission and excitation spectra were recorded in front-face mode with an Edinburgh Instruments FLS 920 fluorescence spectrophotometer. Single crystals were squeezed between two quartz plates (Suprasil) or the powdered sample was mounted in a quartz cuvette with 1 mm path length (similar to the DRS measurements). Measurements were performed in front face reflection mode, with a 400 nm long pass glass filter used for any signal above 410 nm to avoid second order excitation interference. The acquired signal was corrected for the transmittance of this filter.

Low Temperature PL Spectroscopy. We mounted the sample on an insert in a He bath cryostat in which the temperature can be varied from 20 to 300 K. The sample was excited by a solid-state laser operating at 365nm via a 400 m core optical fiber. The PL spectra were collected in the increment of 5K by six similar optical fibers surrounding the excitation fiber coupled to a 0.25 m spectrometer with an intensified charge-coupled-device detector. Photon integration was performed using a multichannel InGaAs diode array where the integration time was set to 10 ms for the whole temperature range.

Raman Scattering Experiments. The infrared Raman measurement (808nm) were carried out using a XY-Dilor spectrometer associated to a Ti-Sapphire (Ti:Al2O3) tunable laser which was pumped by an Argon laser. The pre-monochromator was slightly shifted in order to approach the Rayleigh line by 20 cm^{-1}. At this wavelength, the sample is transparent and no heating effect has been observed. We have used a long working distance ×40 objective with a numerical aperture of 0.4 and selected a laser power under objective of 3 mW. A PI micro-cryostat able to monitor the sample temperature was set temperature to 80 K. One face of the sample was deposited on a thermal conductive glass. Several spectral windows (typically 3) are required and have been merged giving the reported Raman spectra. Raman spectroscopy using visible wavelengths 458, 488 and 514 nm was performed on a home-made system, employing a tubale argon ion laser which is coupled into an inverted Olympus IX71 microscope. Back-scattered light is passed through a TriVista triple spectrometer setup (Princeton Instruments) which used to disperse optical signals that are detected using a liquid nitrogen-cooled CCD camera. Polarisation measurement were performed via Fresnel rhomb and linear polarising combination before optical backscattering, and liner polariser implemented prior to dispersion. Given the high optical absorbance at these wavelengths, relatively low laser powers were employed to avoid laser damage (typically less than 100 W/cm^2).

Computational methods. *Aron and Ruoxi to provide details here...*

[1] Chen, Q., De Marco, N., Yang, Y., Song, T. B., Chen, C. C., Zhao, H., Hong, Z., Zhou, H. & Yang, Y. Under the spotlight: The organic-inorganic hybrid halide perovskite for optoelectronic applications. *Nano Today* **10**, 355–396 (2015).

[2]Yang, W. S., Park, B. W., Jung, E. H., Jeon, N. J., Kim, Y. C., Lee, D. U., Shin, S. S., Seo, J., Kim, E. K., Noh, J. H. & Seok, S. I. Iodide management in formamidinium-lead-halide-based perovskite layers for efficient solar cells. *Science (80-.).* **356**, 1376–1379 (2017).

[3]Green, M. A., Hishikawa, Y., Dunlop, E. D., Levi, D. H., Hohl-Ebinger, J. & Ho-Baillie, A. W. Solar cell efficiency tables (version 51). *Prog. Photovoltaics Res. Appl.* **26**, 3–12 (2018). 1303.4604.

[4]Volonakis, G., Filip, M. R., Haghighirad, A. A., Sakai, N., Wenger, B., Snaith, H. J. & Giustino, F. Lead-Free Halide Double Perovskites via Heterovalent Substitution of Noble Metals. *J. Phys. Chem. Lett.* **7**, 1254–1259 (2016). 1603.01585.

[5]Greul, E., Petrus, M., Binek, A., Docampo, P. & Bein, T. Highly stable, phase pure Cs ₂ AgBiBr ₆ double perovskite thin films for optoelectronic applications. *J. Mater. Chem. A* **00**, 1–10 (2017). 1612.08814.

[6]Pan, W., Wu, H., Luo, J., Deng, Z., Ge, C., Chen, C., Jiang, X., Yin, W.-J., Niu, G., Zhu, L., Yin, L., Zhou, Y., Xie, Q., Ke, X., Sui, M. & Tang, J. Cs2AgBiBr6 single-crystal X-ray detectors with a low detection limit. *Nat. Photonics* 1–8 (2017).

[7]Creutz, S. E., Crites, E. N., De Siena, M. C. & Gamelin, D. R. Colloidal nanocrystals of lead-free double-perovskite (elpasolite) semiconductors: synthesis and anion exchange to access new materials. *Nano Lett.* acs.nanolett.7b04659 (2018).

[8]Savory, C. N., Walsh, A. & Scanlon, D. O. Can Pb-Free Halide Double Perovskites Support High-Efficiency Solar Cells? *ACS Energy Lett.* **1**, 949–955 (2016).

[9]Slavney, A. H., Hu, T., Lindenberg, A. M. & Karunadasa, H. I. A Bismuth-Halide Double Perovskite with Long Carrier Recombination Lifetime for Photovoltaic Applications. *J. Am. Chem. Soc.* **138**, 2138–2141 (2016).

[10]Xiao, Z., Meng, W., Wang, J. & Yan, Y. Thermodynamic Stability and Defect Chemistry of Bismuth-Based Lead-Free Double Perovskites. *ChemSusChem* **9**, 2628–2633 (2016).

[11]Du, K. Z., Meng, W., Wang, X., Yan, Y. & Mitzi, D. B. Bandgap Engineering of Lead-Free Double Perovskite Cs2AgBiBr6through Trivalent Metal Alloying. *Angew. Chemie - Int. Ed.* **56**, 8158–8162 (2017).

[12]Petritz, R. L. & Scanlon, W. W. Mobility of electrons and holes in the polar crystal, PbS. *Phys. Rev.* **97**, 1620–1626 (1955).

[13]Haque, E. & Hossain, M. A. Origin of ultra-low lattice thermal conductivity in Cs 2 BiAg X 6 (X =Cl, Br) and its impact on thermoelectric performance. *J. Alloys Compd.* **748**, 63–72 (2018).

[14]Miyata, K., Meggiolaro, D., Trinh, M. T., Joshi, P. P., Mosconi, E., Jones, S. C., De Angelis, F., Zhu, X.-Y. Y., Tuan Trinh, M., Joshi, P. P., Mosconi, E., Jones, S. C., De Angelis, F. & Zhu, X.-Y. Y. Large polarons in lead halide perovskites. *Sci. Adv.* **3**, e1701217 (2017).

[15]Zhu, X. Y. & Podzorov, V. Charge Carriers in Hybrid Organic-Inorganic Lead Halide Perovskites Might Be Protected as Large Polarons (2015). arXiv:1507.02179v1.

[16]Miyata, K., Atallah, T. L. & Zhu, X. Y. Lead halide perovskites: Crystal-liquid duality, phonon glass electron crystals, and large polaron formation (2017).

[17]Iaru, C. M., Geuchies, J. J., Koenraad, P. M., Vanmaekelbergh, D. & Silov, A. Y. Strong Carrier-Phonon Coupling in Lead Halide Perovskite Nanocrystals. *ACS Nano* **11**, 11024–11030 (2017).

[18]Fu, J., Xu, Q., Han, G., Wu, B., Huan, C. H. A., Leek, M. L. & Sum, T. C. Hot carrier cooling mechanisms in halide perovskites. *Nat. Commun.* **8** (2017).

[19]Wright, A. D., Verdi, C., Milot, R. L., Eperon, G. E., Pérez-Osorio, M. A., Snaith, H. J., Giustino, F., Johnston, M. B. & Herz, L. M. Electron-phonon coupling in hybrid lead halide perovskites. *Nat. Commun.* **7** (2016).

[20]Sendner, M., Nayak, P. K., Egger, D. A., Beck, S., Müller, C., Epding, B., Kowalsky, W., Kronik, L., Snaith, H. J., Pucci, A. & Lovrinčić, R. Optical Phonons in Methylammonium Lead Halide Perovskites and Implications for Charge Transport. *Mater. Horizons* **3**, 1–8 (2016). 1607.08541.

[21]Saran, R., Heuer-Jungemann, A., Kanaras, A. G. & Curry, R. J. Giant Bandgap Renormalization and ExcitonPhonon Scattering in Perovskite Nanocrystals. *Adv. Opt. Mater.* **5** (2017).

[22]Frost, J. M., Whalley, L. D. & Walsh, A. Slow Cooling of Hot Polarons in Halide Perovskite Solar Cells. *ACS Energy Lett.* **2**, 2647–2652 (2017). 1708.04158.

[23]McClure, E. T., Ball, M. R., Windl, W. & Woodward, P. M. Cs2AgBiX6(X = Br, Cl): New Visible Light Absorbing, Lead-Free Halide Perovskite Semiconductors. *Chem. Mater.* **28**, 1348–1354 (2016).

[24]Filip, M. R., Hillman, S., Haghighirad, A. A., Snaith, H. J. & Giustino, F. Band Gaps of the Lead-Free Halide Double Perovskites Cs ₂ BiAgCl ₆ and Cs ₂ BiAgBr ₆ from Theory and Experiment. *J. Phys. Chem. Lett.* **7**, 2579–2585 (2016).

[25]Ke, X., Yan, J., Zhang, A., Zhang, B. & Chen, Y. Optical band gap transition from direct to indirect induced by organic content of CH ₃ NH ₃ PbI ₃ perovskite films. *Appl. Phys. Lett.* **107**, 091904 (2015).

[26]Yang, J., Zhang, P. & Wei, S.-H. Band Structure Engineering of Cs ₂ AgBiBr ₆ Perovskite through OrderDisordered Transition: A First-Principle Study. *J. Phys. Chem. Lett.* **9**, 31–35 (2018).

[27]Filip, M. R., Liu, X., Miglio, A., Hautier, G. & Giustino, F. Phase Diagrams and Stability of Lead-Free Halide Double Perovskites Cs2BB'X6, B = Sb, Bi, B' = Cu, Ag, Au and X = Cl, Br, i. *J. Phys. Chem. C* acs.jpcc.7b10370 (2017).

[28]Smit, W. M., Dirksen, G. J. & Stufkens, D. J. Infrared and Raman spectra of the elpasolites Cs2NaSbCl6and Cs2NaBiCl6: Evidence for a pseudo Jahn-Teller distorted ground state. *J. Phys. Chem. Solids* **51**, 189–196 (1990).

[29]Krylov, A. S., Vtyurin, A. N., Bulou, A. & Voronov, V. N. Raman spectra and phase transitions in the Rb2KScF6 elpasolite. In *Ferroelectrics*, vol. 284, 47–64 (2003).

[30]Papatheodorou, G. N. Raman spectroscopic studies of yttrium (III) chloridealkali metal chloride melts and of Cs ₂ NaYCl ₆ and YCl ₃ solid compounds. *J. Chem. Phys.* **66**, 2893–2900 (1977).

[31]de Jong, M., Seijo, L., Meijerink, A. & Rabouw, F. T. Resolving the ambiguity in the relation between Stokes shift and HuangRhys parameter. *Phys. Chem. Chem. Phys.* **17**, 16959–16969 (2015). _barata Materials and Techniques of polychrome wooden sculpture.

[32]Artús, L., Cuscó, R., Martín, J. M. & González-Díaz, G. Up to fifth-order Raman scattering of InP under nonresonant conditions. *Phys. Rev. B* **50**, 11552–11555 (1994).

[33]Zhang, Q., Zhang, J., Utama, M. I., Peng, B., De La Mata, M., Arbiol, J. & Xiong, Q. Exciton-phonon coupling in individual ZnTe nanorods studied by resonant Raman spectroscopy. *Phys. Rev. B - Condens. Matter Mater. Phys.* **85**, 085418 (2012).

[34]Zeyher, R. Theory of multiphonon raman spectra above the energy gap in semiconductors. *Solid State Commun.* **16**, 49–52 (1975).

[35]Rudin, S. & Reinecke, T. L. Temperature-dependent exciton linewidths in semiconductor quantum wells. *Phys. Rev. B* **41**, 3017–3027 (1990).

[36]Fang, H.-h., Wang, F., Adjokatse, S., Zhao, N., Even, J. & Loi, M. A. Photoexcitation dynamics in solution- processed formamidinium lead iodide perovskite thin films for solar cell applications Running Title : Optical properties of a hybrid perovskite. *Light Sci. Appl.* **5**, e16056–7 (2016).

[37]Yu, P. D. P. Y., Dr, P. & Cardona, D. h. c. M. Vibrational Properties of Semiconductors, and Electron-Phonon Interactions. In *Fundam. Semicond.*, 107–158 (2010).

[38]Frost, J. M. Calculating polaron mobility in halide perovskites. *Phys. Rev. B* **96** (2017). 1704.05404.

[39]Zhao, X. G., Yang, J. H., Fu, Y., Yang, D., Xu, Q., Yu, L.,

Wei, S. H. & Zhang, L. Design of Lead-Free Inorganic Halide Perovskites for Solar Cells via Cation-Transmutation. *J. Am. Chem. Soc.* **139**, 2630–2638 (2017). 1705.10014.

[40] Biaggio, I. Mobility of an electron in a multimode polar lattice. *Phys. Rev. B - Condens. Matter Mater. Phys.* **60**, 299–307 (1999).

[41] Wang, Y., Guan, X., Li, D., Cheng, H. C., Duan, X., Lin, Z. & Duan, X. Chemical vapor deposition growth of single-crystalline cesium lead halide microplatelets and heterostructures for optoelectronic applications. *Nano Res.* **10**, 1223–1233 (2017).

[42] Li, T., Dunlap-Shohl, W. A., Han, Q. & Mitzi, D. B. Melt Processing of Hybrid Organic-Inorganic Lead Iodide Layered Perovskites. *Chem. Mater.* **29**, 6200–6204 (2017).

[43] Dang, Y., Ju, D., Wang, L. & Tao, X. Recent progress in the synthesis of hybrid halide perovskite single crystals. *CrystEngComm* **18**, 4476–4484 (2016).

[44] Neukirch, A. J., Nie, W., Blancon, J. C., Appavoo, K., Tsai, H., Sfeir, M. Y., Katan, C., Pedesseau, L., Even, J., Crochet, J. J., Gupta, G., Mohite, A. D. & Tretiak, S. Polaron stabilization by cooperative lattice distortion and cation rotations in hybrid perovskite materials. *Nano Lett.* **16**, 3809–3816 (2016).

[45] Santomauro, F. G., Grilj, J., Mewes, L., Nedelcu, G., Yakunin, S., Rossi, T., Capano, G., Al Haddad, A., Budarz, J., Kinschel, D., Ferreira, D. S., Rossi, G., Tovar, M. G., Grolimund, D., Samson, V., Nachtegaal, M., Smolentsev, G., Kovalenko, M. V. & Chergui, M. Localized holes and delocalized electrons in photoexcited inorganic perovskites: Watching each atomic actor by picosecond X-ray absorption spectroscopy. *Struct. Dyn.* **4** (2017). 1610.02231.

[46] Guzelturk, B., Belisle, R. A., Smith, M. D., Bruening, K., Prasanna, R., Yuan, Y., Gopalan, V., Tassone, C. J., Karunadasa, H. I., McGehee, M. D. & Lindenberg, A. M. Terahertz Emission from Hybrid Perovskites Driven by Ultrafast Charge Separation and Strong Electron-Phonon Coupling. *Adv. Mater.* 1704737 (2018).

[47] Eßer, F., Drachenko, O., Patanè, A., Ozerov, M., Winnerl, S., Schneider, H. & Helm, M. Direct determination of the electron effective mass of GaAsN by terahertz cyclotron resonance spectroscopy. *Appl. Phys. Lett.* **107** (2015).

Acknowledgements: The authors acknowledge financial support from the Research Foundation-Flanders (FWO, Grant Nos. G.0962.13, G.0B39.15, and G.0197.11, postdoctoral fellowship to J.A.S., H.Y. and E.D.), KU Leuven Research Fund (C14/15/053), the Hercules foundation (HER/11/14), and the Belgian Federal Science Policy Office (IAP-VII/05). The research leading to these results has received funding from the European Research Council under the European Unions Seventh Framework Programme (FP/2007-2013)/ERC Grant Agreement (Grant No. 307523), ERC-Stg LIGHT to M.B.J.R. C.W.K and H.H. acknowledge the Pohang Light Source, Korea, for the use of their diffractometers and computing facilities.

Author contributions: J.A.S. conceived and directed this study. E.D., H.Y. and S.B. grew samples and completed the excitation and emission spectroscopy. C.W.K. and H.H. performed the single crystal x-ray diffraction measurements, J.A.S and P.P. conducted the Raman experiments, M.K. and J.V. completed the low temperature PL studies, and R.X.Y and A.W. performed the first principals calculations. J.A.S., M.K., H,Y., J.H. and M.B.J.R. provided the data analysis and interpretation, while J.A.S. wrote the manuscript. All authors contributed to the discussion and revising of the manuscript.

Additional Information: Supporting Information accompanies this paper.

Competing financial interests: The authors declare there are no competing financial interests pertaining to this work.

TOC image

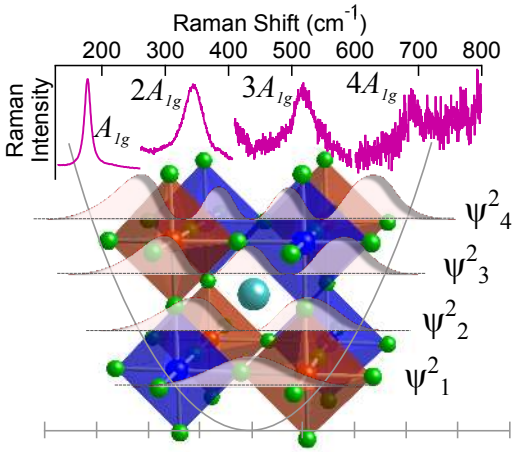
Raman Shift (cm-1)
200
300
400
500
600
700
800
Raman Intensity
A1g
2A1g
3A1g
4A1g
ψ2 4
ψ2 3
ψ2 2
ψ2 1